Journal of Manufacturing Processes 106 (2023) 465–479

Contents lists available at ScienceDirect

Journal of Manufacturing Processes

journal homepage: www.elsevier.com/locate/manpro

Keyhole mode wobble laser welding of a nickel base superalloy - Modeling, experiments, and process maps

Tuhin Mukherjee [a], Mingze Gao [b], Todd A. Palmer [a,b], Tarasankar DebRoy [a,*]

[a] Department of Materials Science and Engineering, Pennsylvania State University, University Park, PA 16802, USA
[b] Department of Engineering Science and Mechanics, Pennsylvania State University, University Park, PA 16802, USA

ARTICLE INFO

Keywords:
Oscillating beam welding
Laser melting
Heat transfer and fluid flow
Power density
Cooling rates
Dendrite arm spacing

ABSTRACT

Keyhole mode wobble laser welding is gaining increasing acceptance due to its ability to bridge gaps, refine microstructure, and enhance the mechanical properties of welds. However, the impact of amplitude, frequency, welding speed, laser beam power, and beam radius on the heat flux distribution, melting pattern, and three-dimensional temperature field is not well understood. To address this need, here we report a combined experimental and computational study to investigate the effects of the key wobble welding parameters on the energy distribution impinging on the welding track, keyhole formation, three-dimensional fluid flow and heat transfer during wobble laser welding of Inconel 740H. The modeling results were rigorously tested using experiments in which the welding speed, laser power, and wobble amplitude and frequency were varied. A bimodal power density distribution with higher power density near the edge than in the middle of the track occurred when the wobble amplitude significantly exceeded the laser beam diameter. A high wobble amplitude resulted in a wide and shallow pool while the wobble frequency used in this work did not significantly impact the fusion zone geometry. A set of process maps were constructed to understand the role of wobble laser parameters in achieving a desirable fusion zone geometry during keyhole mode wobble laser welding. Finally, wobble laser welding with a high amplitude was found to favor rapid solidification and the formation of finer solidification microstructure.

1. Introduction

Keyhole-mode wobble laser welding engages the oscillation of a laser beam often rapidly traversing along circular paths with a high frequency while moving along a linear welding track (Fig. 1). The circular movement of the beam distributes the laser energy over a large area and affects the fusion zone geometry. This technique can improve gap bridgability [1] and weldability [2], refine microstructures [3], achieve superior mechanical properties [4,5], promote the formation of equiaxed grains [5,6], minimize porosity [7,8] and cracking [9] and facilitate dissimilar alloy welding [10]. Because of these advantages, the technique is gaining increasing acceptability in the manufacturing industry. However, many welding parameters such as wobble amplitude, frequency, laser power, scanning speed, laser beam radius, and the thermophysical properties of the alloy affect the power distribution patterns, fusion zone geometry, and the temperature field. The oscillation of the laser beam can alter the energy distribution, leading to significant variations in the temperature fields and fusion zone shape and size. Currently, there is no framework other than trial-and-error testing to select the wobble welding variables to control fusion zone geometry, the temperature field, cooling rates, and microstructure. Thus, there is a need to develop a better understanding of the effects of wobble welding parameters during keyhole mode wobble laser welding of important alloys.

Nickel-based superalloys are commonly used in high-temperature applications such as gas turbines, jet engines, and nuclear reactors due to their excellent mechanical properties and corrosion resistance. An important alloy in this class is Inconel 740H which is a precipitation hardenable alloy containing significant amounts of chromium, cobalt, and smaller concentrations of other alloying elements in nickel. Modeling the effects of key wobble welding parameters on laser energy distribution, fusion zone geometry, fluid flow, and three-dimensional heat transfer during keyhole mode wobble laser welding of Inconel 740H can provide insight into the welding process. Because of the complexity of the physical processes, some simplifications have been made to understand the process and the weld. For example, statistical regression has been used to correlate fusion zone geometry with processing variables [11]. The approach is valid only for the range of

* Corresponding author.
E-mail address: rtd1@psu.edu (T. DebRoy).

https://doi.org/10.1016/j.jmapro.2023.10.017
Received 25 May 2023; Received in revised form 3 September 2023; Accepted 8 October 2023
Available online 14 October 2023

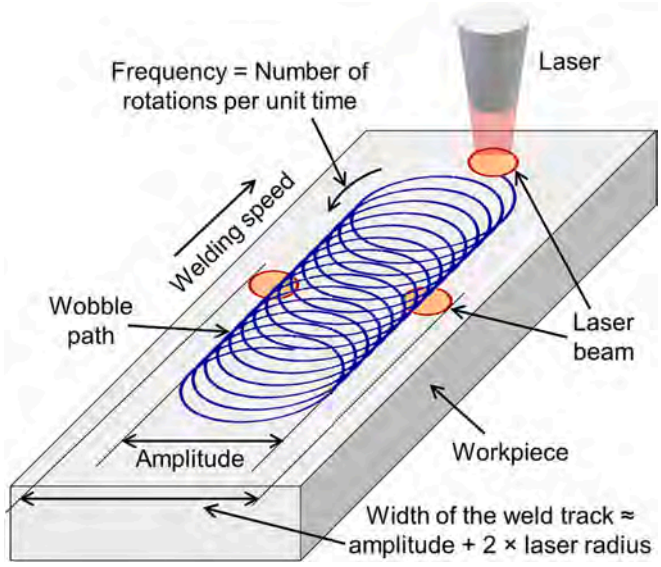

Fig. 1. A schematic diagram of wobble laser welding process. The circular wobble path is shown in blue. The width of the circular wobble path is called the amplitude. The width of the weld track is roughly equal to the summation of the amplitude and twice the laser beam radius. The number of rotations of the laser beam along the circular path per unit time is called the frequency. (For interpretation of the references to color in this figure, the reader is referred to the web version of this article.)

process variables investigated and the alloy and does not uncover any scientific insight that often results from research. Heat conduction models have been proposed to understand the fusion zone attributes [12]. However, these investigations do not consider the convective heat transfer which is often the primary mechanism for heat transfer in the fusion zone. Finally, the numerical modeling of the heat and fluid flow of the wobble laser welding is just beginning [13]. The initial work involved the application of a commercial software to understand heat transfer and fluid flow. Apart from the high cost of licensing such software, the customization of all general-purpose packages to adequately represent the complex physics of wobble welding remains a major challenge. In addition, the computational overhead built into flexible commercial software applicable to diverse manufacturing often make these impractical for the keyhole-mode wobble laser welding. We developed a three-dimensional model of heat and fluid flow during keyhole mode wobble laser welding by extending keyhole welding models developed and rigorously tested at Penn State over an extended time [14–17]. The model was tested by conducting experiments for different values of welding speed, laser power, and wobble amplitude and frequency.

Here we investigate the effects of wobble welding parameters on the fusion zone geometry, temperature fields, cooling rates, and the scale of solidification structure during the keyhole-mode wobble laser welding of Inconel 740H. A three-dimensional heat transfer and fluid flow model was used to compute the temperature field and fusion zone shape and size and the simulated results were validated using experiments. Specifically, we examined the effects of the wobble amplitude, frequency, laser power, and welding speed during welding. The effects of wobble parameters on cooling rates during solidification and solidification microstructure of Inconel 740H are also investigated. The results of this study provide insights into the selection of variables during the keyhole-mode wobble laser welding of Inconel 740H. A set of easy-to-use process maps are presented for understanding the role of wobble welding parameters on the fusion zone geometry.

2. Methodology

2.1. Heat transfer and fluid flow model of keyhole mode wobble laser welding

A three-dimensional heat and fluid flow model for the keyhole-mode wobble laser welding was developed, validated with experiments, and used in this research. The model worked in three steps. First, it calculated the spatial distribution of the laser energy density resulting from the wobble movement of the laser beam. Second, a time average of the energy density was estimated and used to predict the keyhole geometry in 3D by performing a heat and pressure balance on the walls of the keyhole. Finally, it computed the 3D temperature and velocity fields considering the main physical process such as 3D heat transfer in the workpiece, melting, flow of molten metal primarily driven by the spatial surface tension gradient, formation of the two-phase solid-liquid mushy zone, and solidification. These three steps are discussed below:

2.1.1. Assumptions

Below are several simplified assumptions made to make heat transfer and fluid flow calculations tractable:

- A quasi-steady state was assumed where the temporal variations in the temperature and velocity fields and molten pool geometry were not explicitly captured [18]. The effects of welding speed were considered by introducing a source term in the energy conservation equation.
- A time-averaged value of the laser power density was taken to calculate the keyhole geometry. The computational approach assumes that the wobble amplitude is not significantly larger than the spot diameter.
- The recoil pressure on the top surface of the molten pool due to the evaporation from the keyhole can create a curved molten pool surface. Here we assumed a flat top surface of the molten pool to simplify the calculations [14].
- Molten metals were assumed to be Newtonian and incompressible.
- Turbulence in the convective flow of molten metal was considered by enhancing the thermal conductivity and viscosity of the liquid [19,20].
- Thermophysical properties of the alloy used were taken as temperature independent for simplicity.
- The temperature inside the keyhole was kept constant at the boiling point of the alloy used. The temperature at which the summation of the equilibrium vapor pressures of all the constituting elements add up to 1 atm was considered as the boiling point of the alloy [21].
- The absorptivity was assumed to be constant ignoring the effects of plasma attenuation and scattering of the laser beam. [14]

2.1.2. Calculation of power density distribution

We calculated the spatial distribution of the laser energy density on the top surface of the workpiece resulting from the wobble movement of the laser beam. The circular wobble movement of the beam distributes the laser energy over a larger area compared with linear movement and thus controls the fusion zone geometry. For a circular wobble path with an amplitude A, frequency f, and welding speed V, the location (x, y) of the laser beam axis at time t is given by:

$$x = \frac{A}{2} cos\ 2\pi ft + Vt \tag{1}$$

$$y = \frac{A}{2} Sin\ 2\pi ft \tag{2}$$

Here, x and y represent the direction along the length and width, respectively. The welding direction is considered the length direction. At a given location of the laser beam axis (x, y), the laser power density (P_d) on the top surface of the workpiece is represented as:

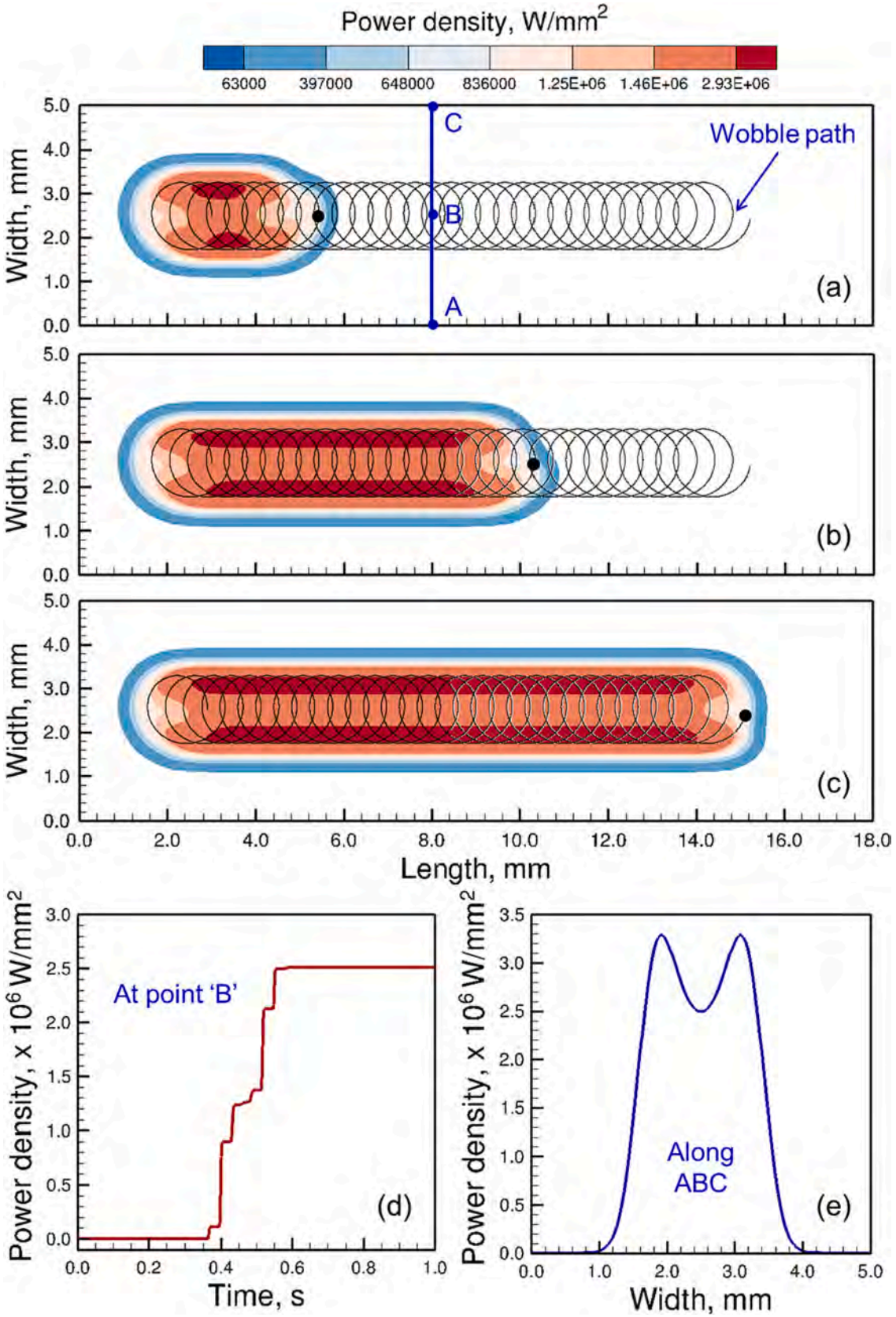

Fig. 2. (a–c) Spatiotemporal variation of laser power density at three different positions of the laser beam axis (shown by black dots on wobble path). (d) Power density at point 'B' shown in figure (a). (e) Time-integrated power density along the path ABC. The results are for 5 kW laser power, welding speed of 12.7 mm/s, 1.6 mm wobble amplitude, and 300 Hz frequency. Other welding parameters are provided in Table 1.

Table 1
Keyhole mode wobble laser welding process variables used in this research.

Process parameters	Values
Laser power (kW)	5, 7.5, 10
Welding speed (mm/s)	12.7, 25.4
Laser beam radius (mm)	0.5
Wobble amplitude (mm)	0.4, 1.6
Wobble frequency (Hz)	150, 300, 411
Workpiece thickness (mm)	12.7

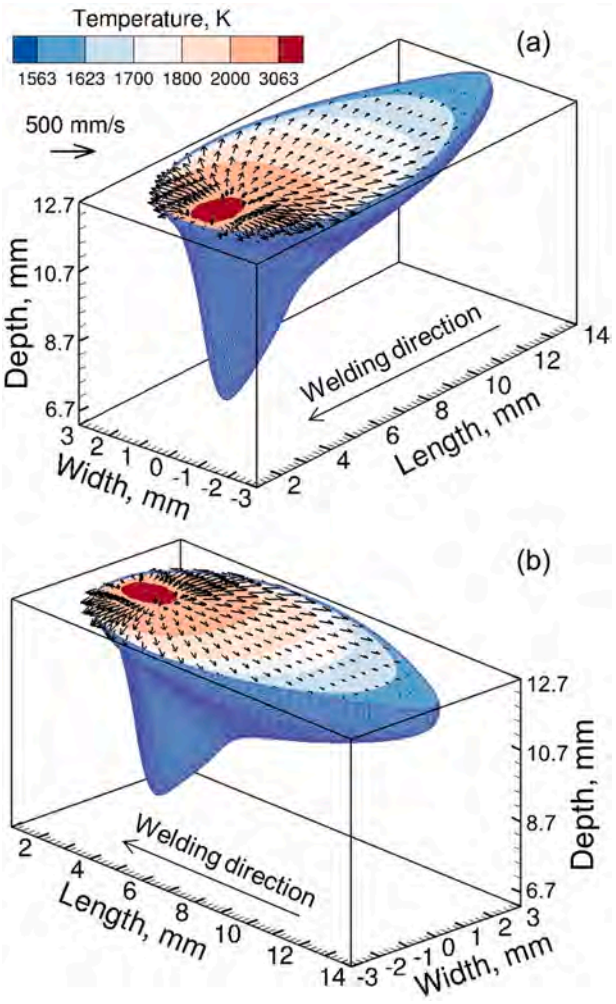

Fig. 3. 3D temperature and velocity distributions during keyhole-mode wobble laser welding of Inconel 740H. Two different 3D isometric views are shown in (a) and (b). The results are for 5 kW laser power, the welding speed of 12.7 mm/s, 0.4 mm wobble amplitude, and 300 Hz frequency. Other welding parameters are provided in Table 1.

$$P_d = \frac{d\,\epsilon\,P}{\pi\, r_b^2} exp\left[-\frac{d\,r^2}{r_b^2}\right] \tag{3}$$

where P is the laser power, r_b is the beam radius, ϵ is the absorptivity, and d is the distribution factor whose value [14–17] is between 1 and 3. The values of the power density are cumulatively added as the laser beam travels along the circular wobble path. Fig. 2 (a–c) show the power density distribution on the top surface of the workpiece at different locations of the laser beam axis along the circular wobble path. The process parameters are reported in Table 1. The circular movement of the laser beam distributes the laser energy over an area that results in significant spatial variations in the power density. In addition, the power density at a given location on the workpiece varies with time during welding. For example, Fig. 2 (d) shows the variation in power density at location 'B' (see Fig. 2 (a)) with time. These spatiotemporal variations are the cause behind the evolution of a wide variety of fusion zone geometry during wobble laser welding. Fig. 2 (e) shows the variation in the power density along the width direction (Along path ABC in Fig. 2 (a)) at the mid-length of the weld. This variation of the power density is a strong function of wobble welding parameters. This power density distribution is taken as an input to predict the keyhole geometry as discussed below.

2.1.3. Prediction of keyhole geometry

In this numerical model, the geometry of keyhole was computed by performing a heat balance as well as pressure balance on a point-by-point basis on the keyhole wall [14,15]. The calculation procedure relied on welding variables and material properties and involved the following steps. First, an initial geometry of keyhole was established by conducting a point-by-point balance of energy [14,15] on the walls of the keyhole, with further details given in the Supplementary Document. The boiling point of the alloy was determined from the equilibrium vapor pressures of all alloying elements versus temperature data [22] and the activities of all alloying elements assuming Roultian behavior near the boiling point [14]. To account for the laser beam's multiple inter-reflections within the keyhole, the number of inter-reflections was calculated using the keyhole geometry [14]. The beam attenuation was computed using a plume attenuation coefficient. The initial keyhole geometry was then adjusted to consider the energy absorption due to multiple reflections and the energy attenuation caused by metal vapor or plasma. Once the initial keyhole geometry had been calculated, the keyhole geometry data was stored in a data file for further analysis.

Next, the temperatures on the keyhole walls were adjusted based on the pressure balance on the wall. Within a stable keyhole region, the vapor pressure tended to sustain the cavity of the vapor, while the hydrostatic pressure and the surface tension worked to close the keyhole. The force balance on the walls of the keyholes was represented as:

$$P_v = P_a + \frac{\gamma(T)}{r(z)} + \rho g z \tag{4}$$

where P_v represents the vapor pressure within the keyhole, P_a represents the surrounding pressure, $\gamma(T)$ refers to the surface tension at the local temperature (T) of the keyhole wall, ρ is the material density, and g is the gravitational acceleration. The function $r(z)$ represents the average keyhole radius at a particular depth z from the top surface, and it is considered half of the keyhole diameter in the welding direction. Using Eq. (4), the vapor pressure at any depth z can be computed based on the recorded data of the keyhole geometry in the initial stage. Afterward, by assuming an ideal solution behavior, the equilibrium temperature versus pressure relation can be utilized to determine the temperature at any given depth along the keyhole walls.

Finally, the modified values for the temperatures along the keyhole wall at all keyhole depths were used to conduct a point by point balance of energy. After that, the pressure and energy balance were performed repeatedly to rectify the keyhole geometry and temperature of the keyhole wall. The iterations were finished when the depth of the keyhole reached an accuracy of 10^{-4} mm.

2.1.4. Computations of 3D temperature and velocity fields

Following the computation of the keyhole's geometry, the resulting profile was transferred to a domain suitable for analyzing heat transfer and fluid flow [14]. The conservation equations of momentum, mass, and energy (see the Supplementary Document) were solved to calculate the 3D temperature and velocity distributions. The conservation equations for heat transfer and fluid flow were solved in three dimensions for the entire workpiece. The governing equations were discretized in a 3D

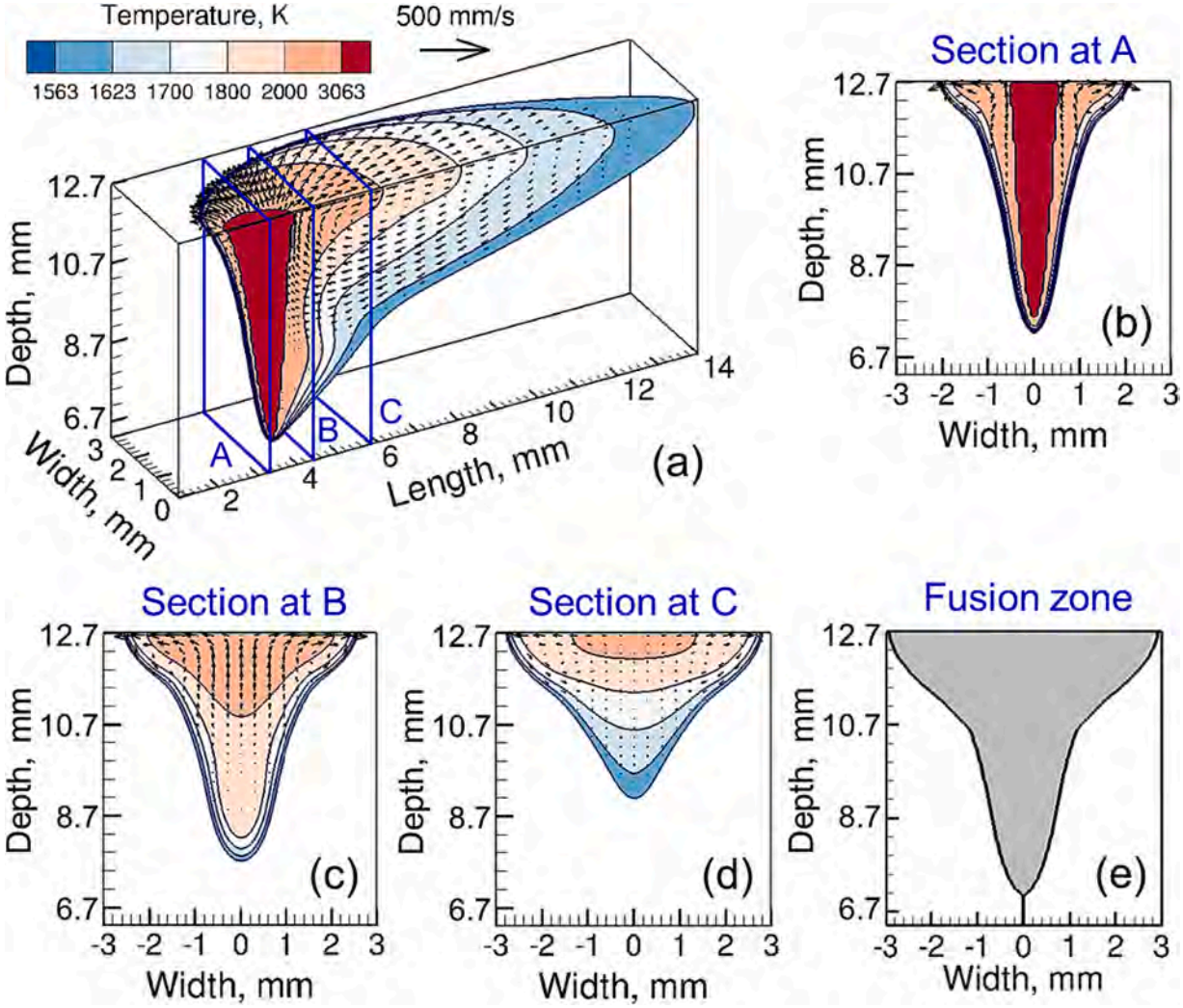

Fig. 4. (a) 3D molten pool geometry showing a cut view of a longitudinal plane at the mid-width of the weld. Transverse views of the molten pool at (b) section A, (c) section B, and (d) section C. The sections are shown in figure (a). (e) Transverse view of the fusion zone. The results are for 5 kW laser power, the welding speed of 12.7 mm/s, 0.4 mm wobble amplitude, and 300 Hz frequency. Other welding parameters are provided in Table 1.

Cartesian coordinate using the control volume method, where the computational domain was divided into small rectangular control volumes. For the area within the keyhole, the coefficients and source terms in the conservation equations were adjusted to determine the modified temperature of the keyhole's walls at various depths and with no fluid velocity. The governing equations and boundary conditions are documented in the supplementary document. The boundary conditions were applied as follows:

- On the top surface, excluding the area around the keyhole, the boundary condition for velocity was determined by the Marangoni effect. Because there is little outward flow on the top surface, the velocity component along the vertical direction was set to zero. Convective and radiative heat losses were applied as boundary conditions to the conservation equation of energy [14].
- The temperature of the keyhole wall was fixed by assigning an appropriate enthalpy value at a given depth. No mass flux was present due to convection, so the velocity component perpendicular to the keyhole surface was set to zero for the stable keyholes formed under the processing conditions used. Melt flow occurred along the vertical direction as a result of the temperature gradient along the keyhole wall.
- For all other workpiece surfaces, there was no melt flow, so the fluid velocities along all three directions were fixed at zero. In addition, radiation and convective heat transfer boundary conditions were applied [14].

The thermophysical properties of Inconel 740H required in the simulations were calculated using a commercial package JMatPro and are reported in the Supplementary Document. Calculations were performed in the Cartesian coordinate where the welding direction was taken along the X-axis. The numerical model was built by developing an in-house Fortran code that was compiled in an Intel Compiler.

2.2. Experimental procedure

An IPG Photonics® YLR-12000-L ytterbium fiber laser was used to produce multiple welds on 12.7 mm thick plates of Inconel 740H. The laser was supplied with the help of a robotic welding system. The fiber laser system used a focal distance of 150 mm, a fiber diameter of 200 μm, and focusing distance of 600 mm [23]. Approximately 50 mm long welds were fabricated. The laser power was 5 kW, 7.5 kW, and 10 kW and the welding speed ranged from 12.7 mm/s to 25.4 mm/s. A beam diameter of 1.04 mm in sharp focus was used. Rayleigh length and the divergence angle were 29.4 mm and 34.2 milli radian (mrad),

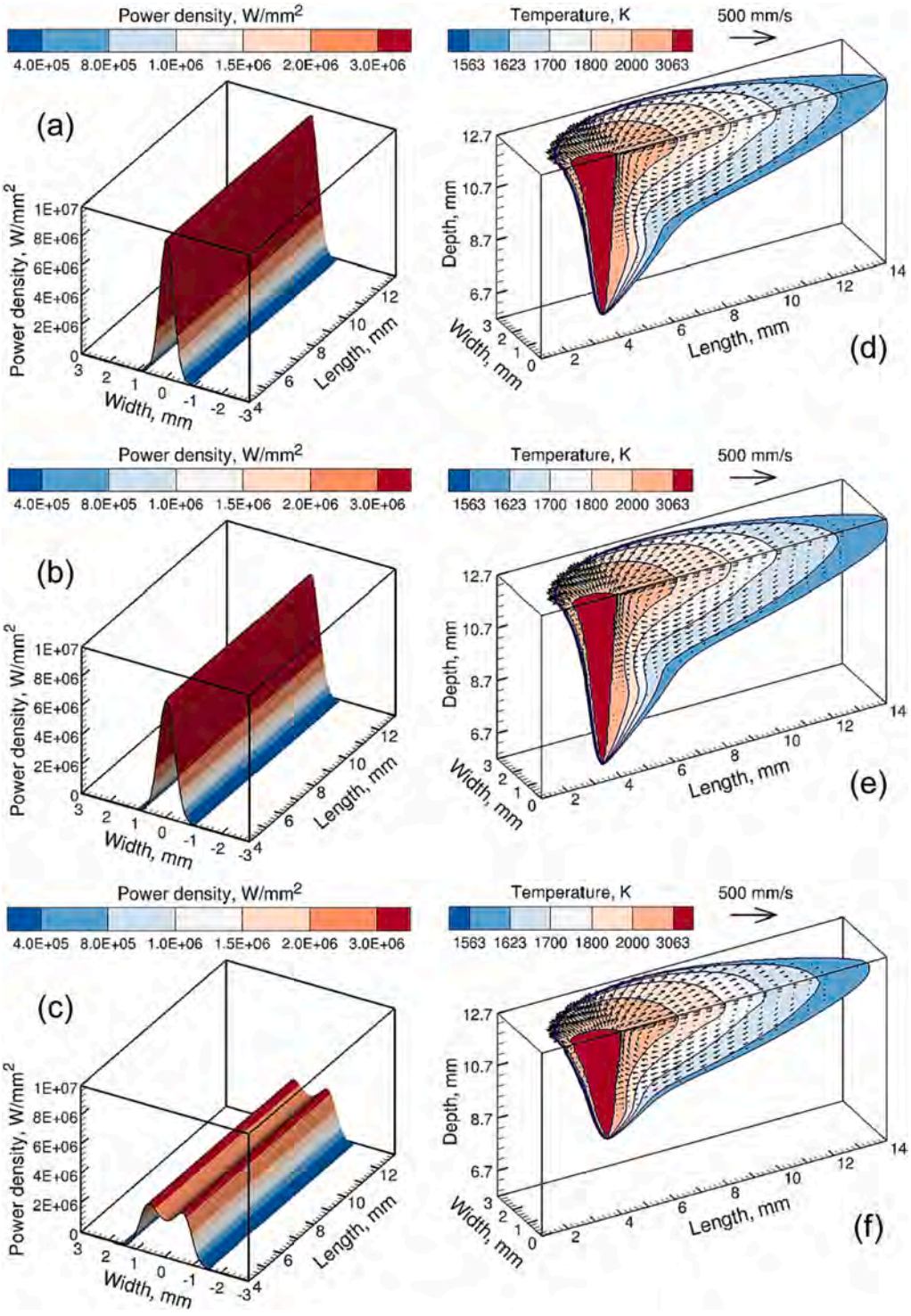

Fig. 5. Variations in power density with amplitude of (a) 0 mm, (b) 0.4 mm, and (c) 1.6 mm. Variations in molten pool geometry with amplitude of (d) 0 mm, (e) 0.4 mm, and (f) 1.6 mm. The results are for 5 kW laser power, the welding speed of 12.7 mm/s, and 150 Hz frequency. Other welding parameters are provided in Table 1.

respectively. A Primes® Focus Monitor measured the beam parameter as 8.9 mm × mrad. A circular wobble pattern [24–26] was used to make the welds where the amplitudes were 0.4 mm and 1.6 mm. In addition, wobble frequencies of 150 Hz, 300 Hz, and 411 Hz were used.

Transverse cross-sections of the weld samples were produced by using the well-known techniques and the samples were polished with a slurry of 1 μm diamond powders. An etchant called the Lucas solution (150 mL HCl + 3 g oxalic acid + 50 mL lactic acid) was used for electrolytic etching of the samples. The etching was performed at an electric potential of 4 V and was continued for several seconds until the boundaries of the fusion zone were clearly visible. A Zeiss optical microscope was used to take several high-resolution images. ImageJ software was used to analyze the images for measuring the weld dimensions. Measurements of weld dimensions were taken at three cross-sections of the welds to report the average and standard deviation values. A scanning electron microscope (SEM) was employed to characterize the solidification microstructure.

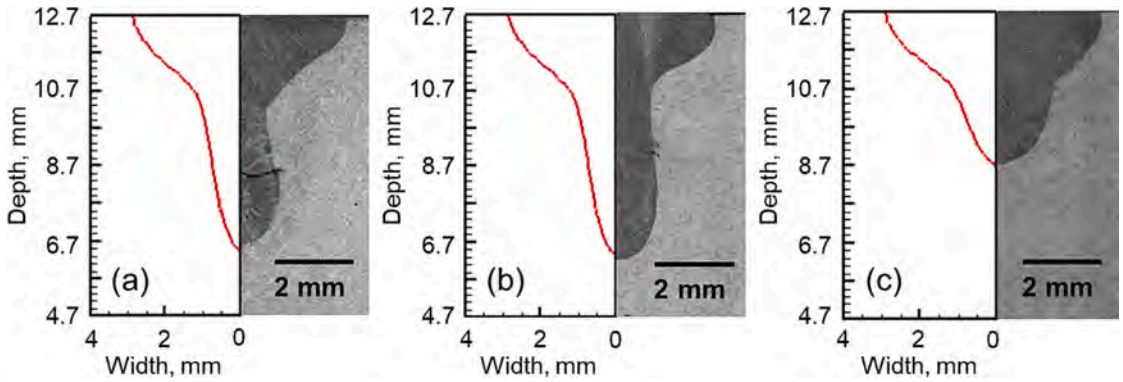

Fig. 6. Comparison between computed and experimentally measured fusion zones for (a) linear welding and for wobble welding with amplitudes of (b) 0.4 mm and (c) 1.6 mm. The results are for 5 kW laser power, the welding speed of 12.7 mm/s, and 150 Hz frequency. Other welding parameters are provided in Table 1.

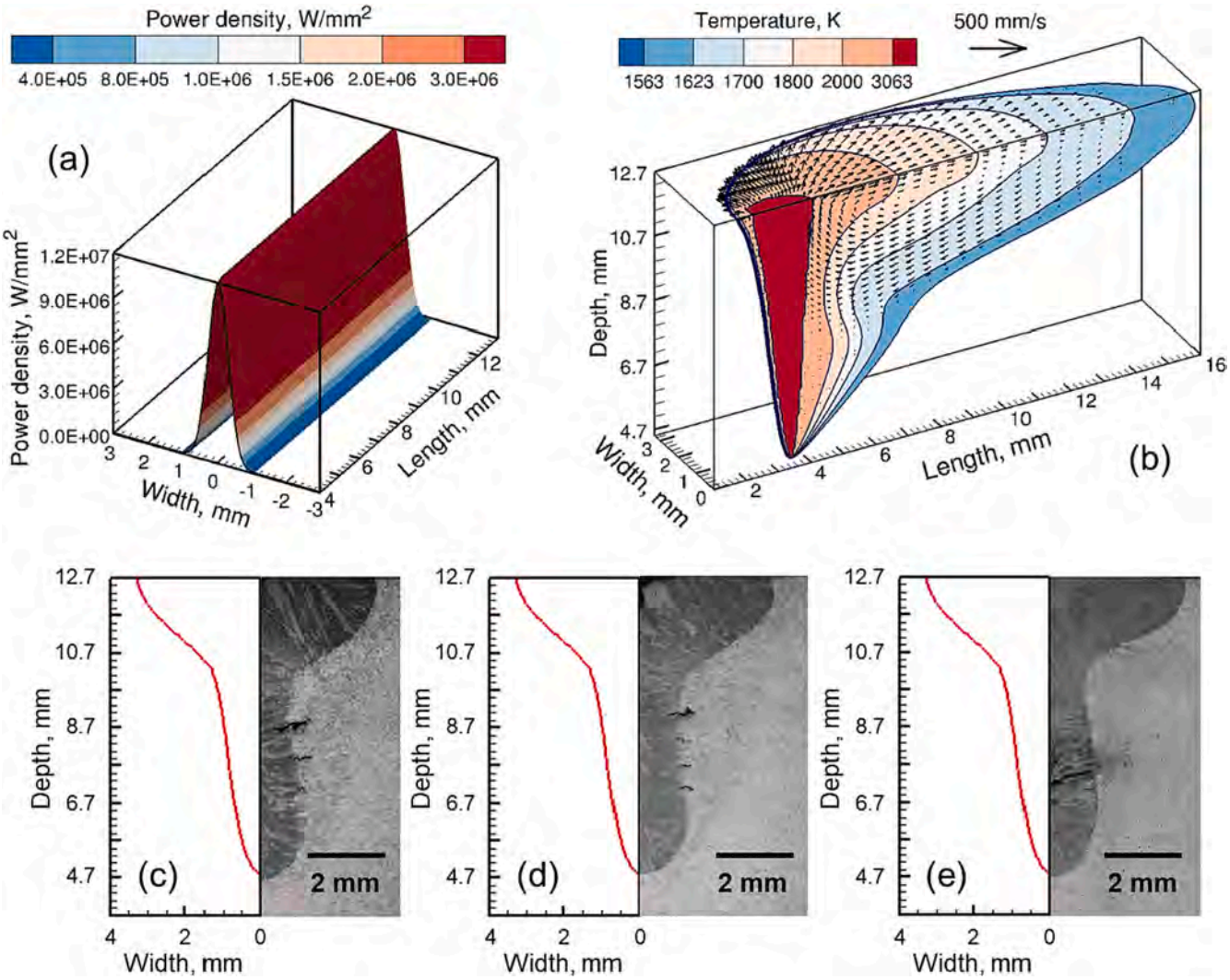

Fig. 7. Variations in power density and molten pool geometry with frequencies. (a) Power density and (b) molten pool are shown at 150 Hz. Since the frequency does not have a significant effect on the power density and molten pool geometry, results for 300 Hz and 411 Hz frequencies are not shown. Comparison between computed and experimentally measured fusion zones at frequencies of (c) 150 Hz, (d) 300 Hz, and (e) 411 Hz. The results are for 7.5 kW laser power, the welding speed of 12.7 mm/s, and 0.4 mm wobble amplitude. Other welding parameters are provided in Table 1.

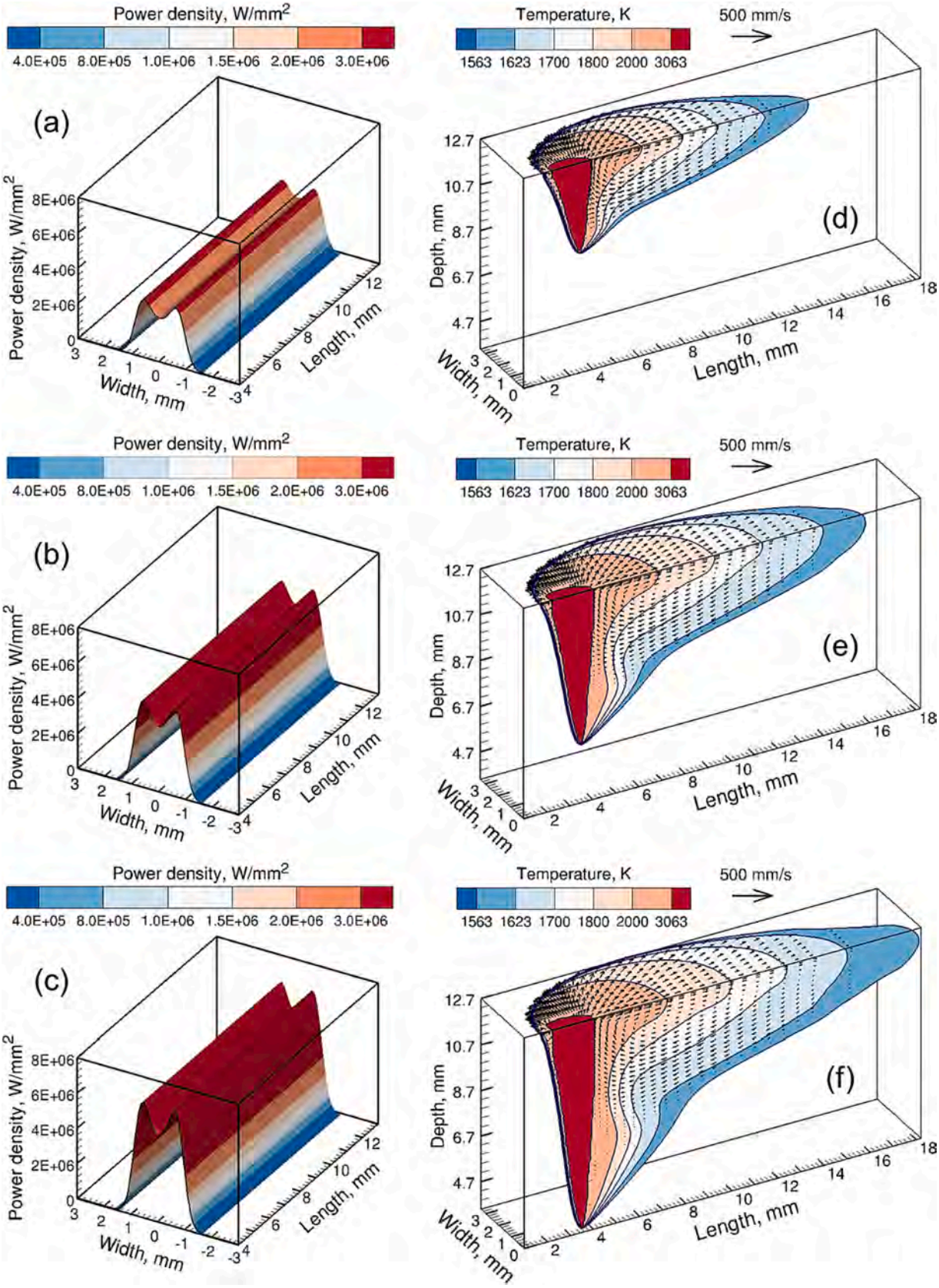

Fig. 8. Variations in power density with laser power of (a) 5 kW, (b) 7.5 kW, and (c) 10 kW. Variations in molten pool geometry with laser power of (d) 5 kW, (e) 7.5 kW, and (f) 10 kW. The results are for 12.7 mm/s welding speed, 1.6 mm wobble amplitude, and 411 Hz frequency. Other welding parameters are provided in Table 1.

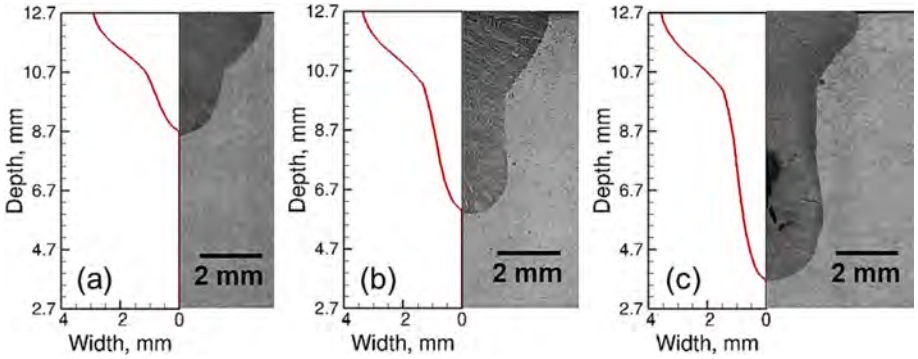

Fig. 9. Comparison between computed and experimentally measured fusion zones at laser powers of (a) 5 kW, (b) 7.5 kW, and (c) 10 kW. The results are for 12.7 mm/s welding speed, 1.6 mm wobble amplitude, and 411 Hz frequency. Other welding parameters are provided in Table 1.

3. Results and discussions

3.1. 3D temperature and velocity fields and fusion zone geometry

The 3D temperature and velocity distributions when the laser beam is positioned at the half-length of the track during the keyhole mode laser wobble welding of Inconel 740H are shown in Fig. 3. In the figure, the region surrounded by the solidus isotherm (1563 K) of Inconel 740H indicates the molten pool. The region between the solidus (1563 K) and liquidus (1623 K) isotherms represents the two-phase mushy zone. The red region bound by the boiling point (3063 K) isotherm is the keyhole. Isotherms are compressed near the front of the molten pool, while they are elongated near the trailing edge due to the welding speed along the length direction. The flow velocity of the liquid material is represented by black vectors. The flow is mainly driven by the spatial surface tension gradient on the molten pool top surface. To find the absolute magnitudes of the velocities, the length of the velocity vectors needs to be compared with the length of the reference vector provided in the figure. The liquid metal flow occurs on the molten pool top surface from the mid-location where surface tension is low (at a high temperature) to the boundary at high surface tension (where the temperature is low). Two different 3D isometric views are shown to emphasize the 3D complex geometry of the molten pool. At the center of the molten pool where a keyhole forms because of the accumulation of high energy, the molten pool shows a deep finger-like penetration depth. In contrast, the molten pool is relatively wider and shallower near the trailing edge. This complex shape of the molten pool controls the fusion zone geometry as explained in Fig. 4.

Fig. 4 (a) shows a 3D isometric cut view of Fig. 3 (a) to reveal the internal features of the molten pool on a longitudinal section along the welding direction. A deep and narrow keyhole bound by the boiling point (3063 K) isotherm can be seen near the front of the molten pool. The transverse sections of the molten pool perpendicular to the welding direction are shown at three different planes (Fig. 4 (b–d)). It can be seen that the depth of the molten pool is the highest near the keyhole and is largely controlled by the keyhole depth (Fig. 4 (b)). However, the pool is the widest in section C (Fig. 4 (d)). The resulting fusion zone geometry (Fig. 4 (e)) forms due to the combined effects of these different cross-sections. The fusion zone depth is the same as the pool depth in section A in Fig. 4 (b) and the width is the same as the pool width in section C in Fig. 4 (d). This unique fusion zone geometry is strongly dependent on the wobble welding parameters as discussed below.

3.2. Effects of wobble amplitude, frequency, laser power, and welding speed

Since the spatiotemporal variations in laser power density and the resulting fusion zone geometry are dependent on the variables wobble amplitude, frequency, laser power, and welding speed, it is important to understand their effects to effectively control the fusion zone geometry.

3.2.1. Wobble amplitude

Fig. 5 shows the variations in the power density distribution and resulting molten pool geometry at different wobble amplitudes for constant laser power, welding speed, and wobble frequency. Since the same laser energy is distributed over a larger area at a higher wobble amplitude, the peak power density is significantly reduced. The peak power density decreases from linear welding (Fig. 5 (a)) to wobble welding with an amplitude of 0.4 mm (Fig. 5 (b)) and 1.6 mm (Fig. 5 (c)). It is interesting to note that the peak power density at 1.6 mm amplitude is observed near the periphery of the wobble path. The decrease in power density at high wobble amplitudes also results in smaller pools with shallower keyholes inside. The molten pool size decreases from linear welding (Fig. 5 (d)) to wobble welding with an amplitude of 0.4 mm (Fig. 5 (e)) and 1.6 mm (Fig. 5 (f)). The calculated fusion zone transverse sections for linear welding as well as for wobble welding at two different wobble amplitudes match well with the corresponding experimental results (Fig. 6) which indicates that the model can effectively capture the effects of wobble amplitude on the variations in laser power density and the resulting pool dimensions and fusion zone geometry.

3.2.2. Wobble frequency

Fig. 7 shows the variations in the power density distribution and resulting molten pool geometry at different wobble frequencies for constant laser power, welding speed, and wobble amplitude. Since the frequencies used in this work do not affect the area within which the laser power is distributed per unit time, it has minimal impact on the power density distribution. Therefore, the molten pool shape and size remain almost unchanged at different wobble frequencies. Since the frequency does not have a significant effect, the power density (Fig. 7 (a)) and molten pool (Fig. 7 (b)) are shown at 150 Hz. The calculated fusion zone transverse sections at three different wobble frequencies match well with the corresponding results from experiments (Fig. 7 (c–e)). Both the computed and experimental results indicate a minimal effect of frequency on fusion zone geometry.

3.2.3. Laser power

Fig. 8 shows the variations in the power density distribution and resulting molten pool geometry at different laser powers for constant welding speed, wobble amplitude, and wobble frequency. The peak power density is proportional to laser power (Fig. 8 (a–c)). For example, the peak power density rises from about 4 MW/mm^2 (Fig. 8 (a)) to about 8 MW/mm^2 (Fig. 8 (c)) when the laser power increases from 5 kW to 10 kW. The increase in the power density at higher laser powers also resulted in larger molten pools with deep keyholes inside (Fig. 8 (d–f)). The calculated fusion zone transverse sections at three different laser powers match well with the corresponding experimental results (Fig. 9). Both the computed and experimental results indicate the formation of deeper keyholes at higher laser powers.

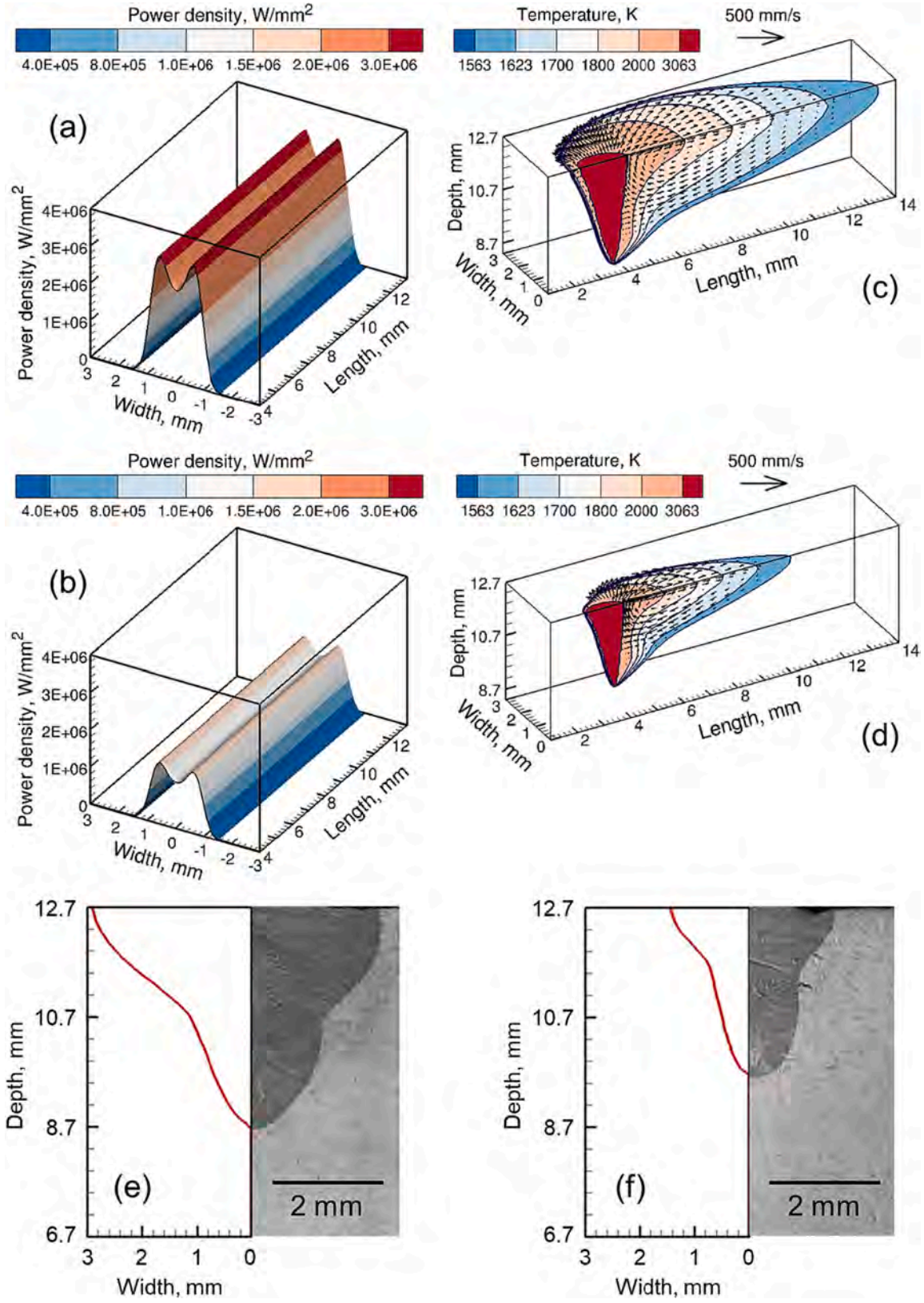

Fig. 10. Variations in power density with welding speed of (a) 12.7 mm/s and (b) 25.4 mm/s. Variations in molten pool geometry with welding speed of (c) 12.7 mm/s and (d) 25.4 mm/s. Comparison between computed and experimentally measured fusion zones at welding speeds of (e) 12.7 mm/s and (f) 25.4 mm/s. The results are for 5 kW laser power, 1.6 mm wobble amplitude, and 300 Hz frequency. Other welding parameters are provided in Table 1.

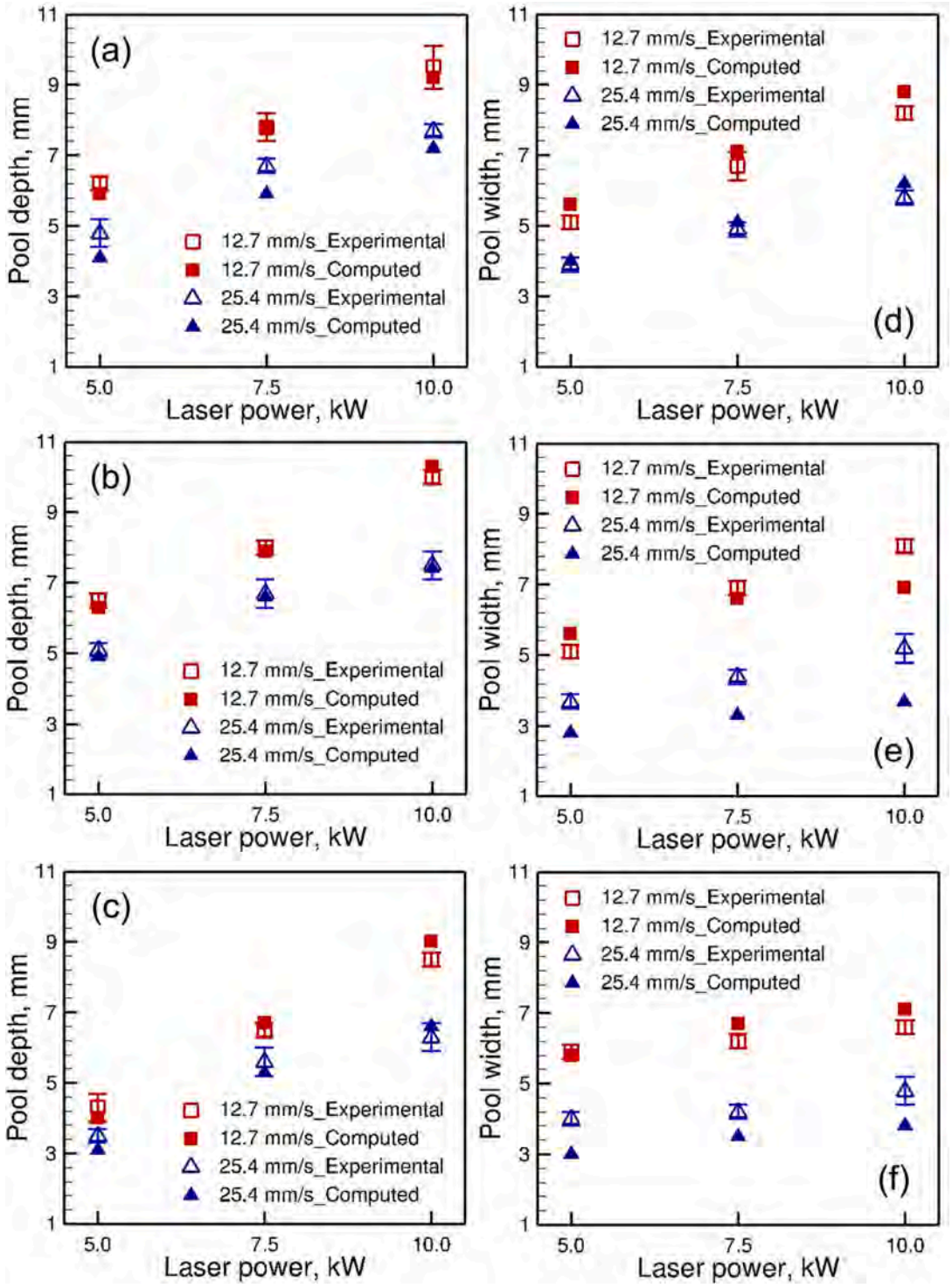

Fig. 11. Comparison between computed and experimentally measured pool depths at different laser powers and welding speeds for (a) linear welding, (b) wobble amplitude of 0.4 mm, and (c) wobble amplitude of 1.6 mm. Comparison between computed and experimentally measured pool widths at different laser powers and welding speeds for (d) linear welding, (e) wobble amplitude of 0.4 mm, and (f) wobble amplitude of 1.6 mm. The results are for 300 Hz frequency. Other welding parameters are provided in Table 1.

3.2.4. Welding speed

Fig. 10 shows the variations in the power density distribution and resulting molten pool geometry at different welding speeds for constant laser power, wobble amplitude, and wobble frequency. A laser beam travels more distance at a higher welding speed increasing the area on which the laser power is distributed. Since the same laser energy is distributed over a larger area at a higher welding speed, the peak power density is significantly reduced. For example, the peak power density decreases from about 3 MW/mm^2 (Fig. 10 (a)) to about 1.5 MW/mm^2 (Fig. 10 (b)) when the welding speed increases from 12.7 mm/s to 25.4 mm/s. The reduction in the power density at higher welding speeds also resulted in smaller molten pools with shallow keyholes inside (Fig. 10 (c–d)). The calculated fusion zone transverse sections match well with the corresponding experimental results (Fig. 10 (e–f)) both indicating

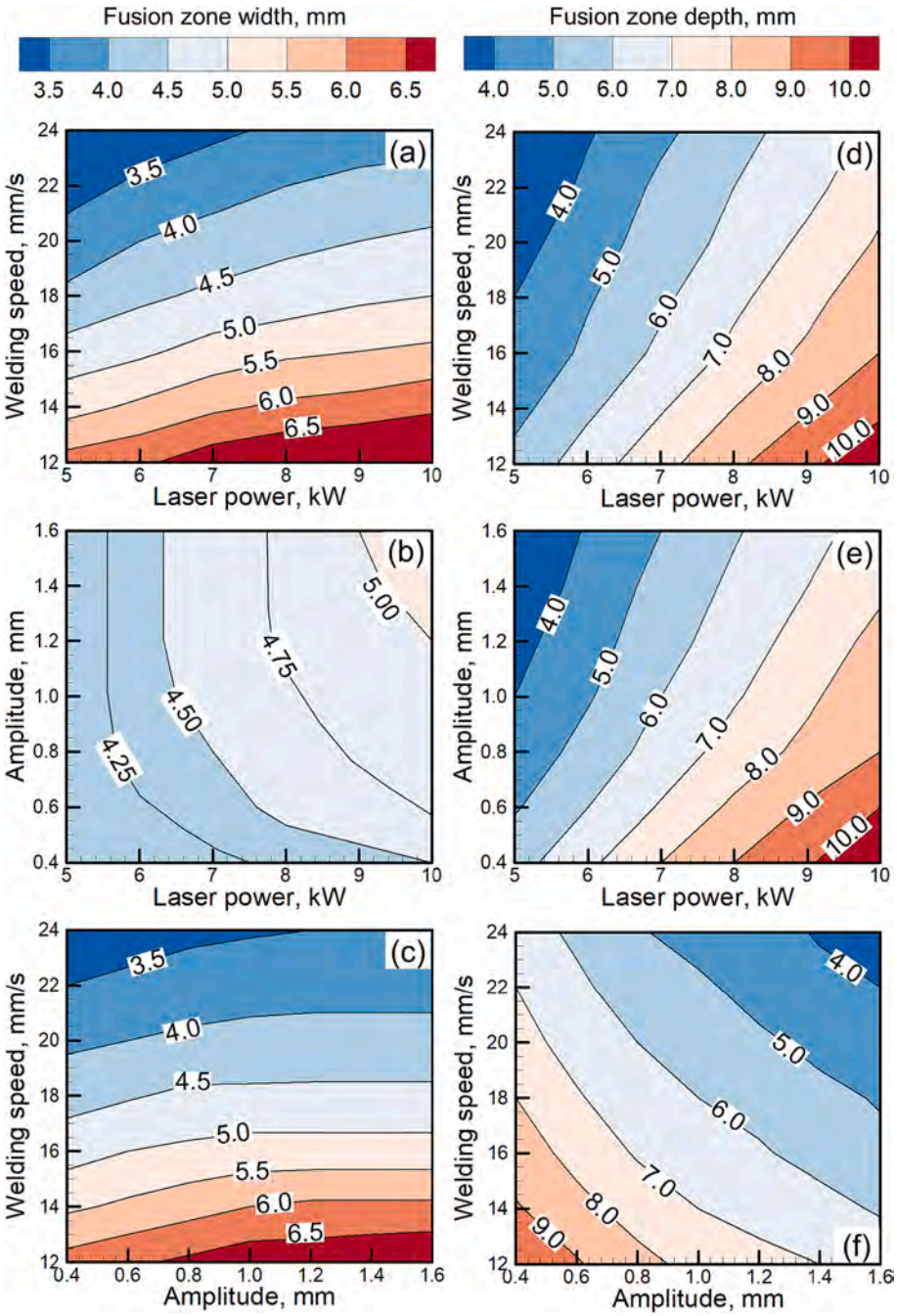

Fig. 12. Process maps for fusion zone width with respect to (a) laser power and welding speed, (b) laser power and wobble amplitude, and (c) welding speed and wobble amplitude. Process maps for fusion zone depth with respect to (d) laser power and welding speed, (e) laser power and wobble amplitude, and (f) welding speed and wobble amplitude. The contour values in the maps represent the fusion zone width and depth in millimeters. For figures (a) and (d), the amplitude is kept constant at 1.0 mm. For figures (b) and (e), the scanning speed is kept constant at 18 mm/s. For figures (c) and (f), laser power is kept constant at 7 kW. For all figures, frequency is kept constant at 300 Hz. Other welding parameters are provided in Table 1.

the formation of narrower and shallower fusion zone at higher welding speeds.

Fig. 11 provides comparisons between computed and experimentally measured pool depths and widths at different laser powers and welding speeds for linear welding as well as for wobble welding with different wobble amplitudes. The good agreement between the computed and experimental results indicates that the model can accurately capture the effects of wobble welding parameters on fusion zone geometry and provides us the confidence to use the well-tested model for constructing process maps as discussed below.

3.3. Process maps for keyhole mode wobble laser welding

Fusion zone width and depth are important in keyhole mode welding. Here we constructed several process maps (Fig. 12) to show how the fusion zone width and depth can be controlled by modifying the wobble welding process parameters. The contour values in the maps represent the fusion zone width and depth in millimeters. Fig. 12 (a) and (d) show process maps of the fusion zone width and depth, respectively for various laser powers and welding speeds. Both width and depth of the fusion zone increase at higher laser power and slower welding speed. For example, an increase in laser power from 5 to 10 kW at a scanning speed

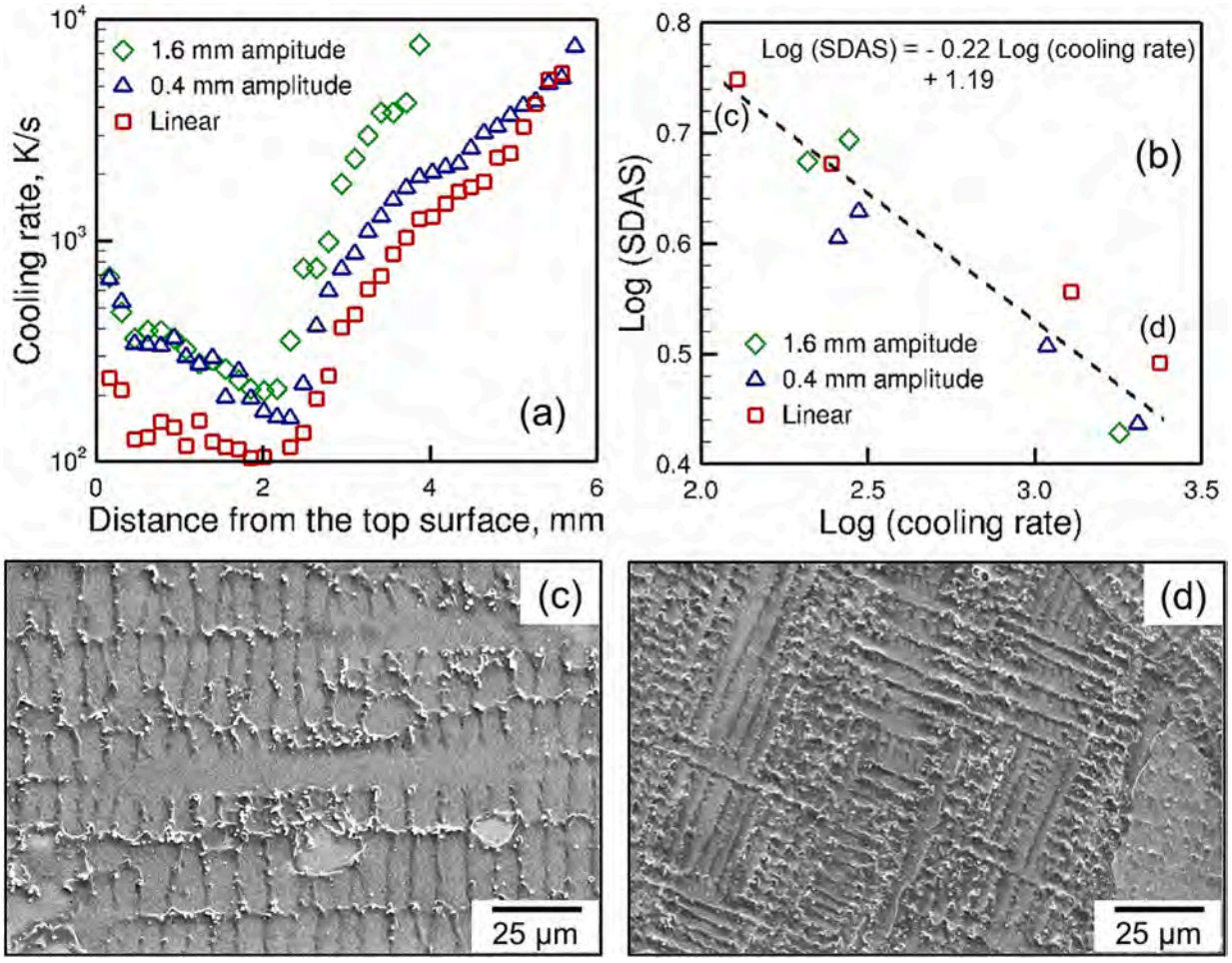

Fig. 13. (a) Variations in cooling rates during solidification along the depth of the workpiece at different wobble amplitudes. The results are for 5 kW laser power, the welding speed of 12.7 mm/s, and 300 Hz frequency. Other welding parameters are provided in Table 1. (b) Linear correlation between the logarithm of secondary dendrite arm spacing (SDAS) and the logarithm of cooling rate during solidification at different wobble amplitudes. The data points are for different laser powers and welding speeds. The frequency is kept constant at 300 Hz. Other welding parameters are provided in Table 1. (c–d) SEM images showing the dendritic solidification microstructure for two cases indicated in figure (b).

of 18 mm/s increases the fusion width and depth by about 1 mm and 4 mm, respectively.

Fig. 12 (b) and (e) show process maps of the fusion zone width and depth, respectively for various laser powers and wobble amplitudes. Both width and depth of the fusion zone increase at higher laser power because of an enhancement in heat input. However, a decrease in power density at high wobble amplitudes results in shallower fusion zones (Fig. 12 (e)). For a given laser spot size, the fusion zone width is almost linearly proportional to amplitude (Fig. 1). However, a high wobble amplitude reduces the power density and tends to decrease the fusion zone width. Because of these two opposing effects, the change in fusion zone width (Fig. 12 (b)) with amplitude is significantly less compared to its effects on fusion zone depth (Fig. 12 (e)). Fig. 12 (c) and (f) show process maps of the fusion zone width and depth, respectively for various scanning speeds and wobble amplitudes. Both low speed and amplitude increase the power density and result in a deeper fusion zone (Fig. 12 (f)). Welding speed has more impact on fusion zone width compared to wobble amplitude as evident from the low horizontal slopes of the contour lines (Fig. 12 (c)). When similar process maps are constructed and tested for diverse materials covering a wide range of processing conditions, they can be useful on the shop floor for selecting appropriate sets of process parameters without trial and error.

3.4. Cooling rates and dendrite arm spacing

Solidification parameters, temperature gradient (G) and solidification growth rate (R), are important because their product (GR) indicates the cooling rate during solidification that affects the solidification microstructures. The difference of the values of the liquidus and solidus temperatures was divided by the mushy zone length to compute the temperature gradient (G). In addition, solidification rates (R) were calculated by multiplying the cosine of the angle of the local solidification direction with the welding speed. Cooling rate (GR) affects the coarsening of the solidification structure, with lower cooling rates leading to coarser microstructures [27]. Fig. 13 (a) showed the comparison of cooling rates obtained along the center longitudinal plane between different wobble conditions under 5 kW laser power and the welding speed of 12.7 mm/s. The temperature gradient increased with higher amplitude due to the decrease in the weld pool length, which shortened the distance between liquidus and solidus isotherms. The solidification rate decreased with higher amplitude since the slope of the solidification front becomes lower near the bottom of the weld pool. Thus, welding with higher amplitudes resulted in faster cooling.

The calculated cooling rate was correlated with the size of the solidification structure, especially the secondary dendrite arm spacing (SDAS). SDAS was measured by locating at least eight consecutive secondary dendrite arms and a minimum of 30 intercepted secondary dendrite arms were measured at selected locations along the build

height. It has been reported [28–30] that there is a linear relationship between log(GR) and log(SDAS), with a theoretical slope varying between −0.5 to −0.2. As shown in Fig. 13 (b–d), the calculated log(GR) values and the experimentally determined log(SDAS) values roughly displayed a linear relationship, and the fitted line has a slope of −0.22. The results indicated that the model can readily capture process conditions during the high-power laser welding process. Using this correlation, the scale of the solidification structure can be estimated with the calculated cooling rate.

4. Summary and conclusions

In this research, we uncovered the effects of wobble welding parameters, laser power, welding speed, amplitude, and frequency, on the laser energy distribution, keyhole formation, and fusion zone geometry during keyhole-mode wobble laser welding of Inconel 740H. We developed, tested, and used a 3D heat transfer and fluid flow model of keyhole mode wobble laser welding. Experiments were performed at different processing conditions to rigorously test the model results. Below are the specific findings:

(1) For a laser beam with a given power and welding speed, the fusion zone geometry can be effectively controlled by adjusting the wobble amplitude. In contrast, the wobble frequency above 150 Hz did not significantly impact the fusion zone geometry because of its minimal effect on the power density distribution. As expected, low power density at a high wobble amplitude resulted in a wide and shallow pool.
(2) When the wobble amplitude was significantly larger than the laser beam diameter, the impinging power density distribution on the welding track showed a bimodal distribution with peak power densities near the edges of the track and lower power density in the middle of the track. A high laser power and slow welding speed resulted in a fusion zone characteristic of a keyhole mode linear welding for the range of wobble amplitude and frequency investigated.
(3) Cooling rate during solidification (GR), where G is the temperature gradient and R is the solidification growth rate, increased with amplitude. Therefore, wobble laser welding was found to favor rapid solidification and the formation of finer solidification microstructure.
(4) Process maps of the fusion zone width and depth constructed in this work proved that the fusion zone width can be increased at a high laser power and wobble amplitude and low welding speed. Thus, the data demonstrate that wobble laser welding at high amplitudes can fill gaps in the mating surfaces of large workpieces. In contrast, a high laser power and low wobble amplitude, and welding speed were found to increase the fusion zone depth. Process maps resulting from this work can be useful on the shop floor for selecting appropriate sets of process parameters without trial and error.

Declaration of competing interest

The authors declare that they have no known competing financial interests or personal relationships that could have appeared to influence the work reported in this paper.

Acknowledgments

The Inconel 740H plate material was provided by Dr. T.M. Lillo at the Idaho National Laboratory. Dr. Lillo also provided many helpful discussions that contributed to the analysis. We also thank Vijay Kancharla and Steven Wirta at IPG Photonics for fabricating the welds. Computations for this research were performed on the Roar supercomputer managed by the Institute for Computational and Data Sciences at Pennsylvania State University. This work was supported by Battelle Energy Alliance, LLC under Contract No. DE-AC07–05ID14517 with the U.S. Department of Energy under Award Number FWP-B100–19010. The publisher, by accepting the paper for publication, acknowledges that the United States Government retains a nonexclusive, paid-up, irrevocable, worldwide license to publish or reproduce the published form of this manuscript, or allow others to do so, for United States Government purposes.

Appendix A. Supplementary data

Supplementary data to this article can be found online at https://doi.org/10.1016/j.jmapro.2023.10.017.

References

[1] Chianese G, Jabar S, Franciosa P, Ceglarek D, Patalano S. A multi-physics CFD study on the part-to-part gap during remote laser welding of copper-to-steel battery tab connectors with beam wobbling. Proc CIRP 2022;111:484–9. https://doi.org/10.1016/j.procir.2022.08.075.
[2] Ramiarison H, Barka N, Pilcher C, Stiles E, Larrimore G, Amira S. Weldability improvement by wobbling technique in high power density laser welding of two aluminum alloys: Al-5052 and Al-6061. J Laser Appl 2021;33(3):032015. https://doi.org/10.2351/7.0000353.
[3] Li J, Sun Q, Liu Y, Zhen Z, Sun Q, Feng J. Melt flow and microstructural characteristics in beam oscillation superimposed laser welding of 304 stainless steel. J Manuf Process 2020;50:629–37. https://doi.org/10.1016/j.jmapro.2019.12.053.
[4] Trushnikov DN, Koleva EG, Mladenov GM, Belenkiy VY. Effect of beam deflection oscillations on the weld geometry. J Mater Process Technol 2013;213(9):1623–34. https://doi.org/10.1016/j.jmatprotec.2013.03.028.
[5] Vázquez L, Huarte I, Galdos L, Álvarez P. Influence of high frequency wobbling parameters on the weld quality of aluminium LBW. Proc CIRP 2022;111:439–42. https://doi.org/10.1016/j.procir.2022.08.183.
[6] Yan F, Qin Y, Tang B, Zhou Y, Gao Z, Hu Y, et al. Effects of beam oscillation on microstructural characteristics and mechanical properties in laser welded steel-copper joints. Optics Laser Technol 2022;148:107739. https://doi.org/10.1016/j.optlastec.2021.107739.
[7] Franco D, Oliveira JP, Santos TG, Miranda RM. Analysis of copper sheets welded by fiber laser with beam oscillation. Optics Laser Technol 2021;133:106563. https://doi.org/10.1016/j.optlastec.2020.106563.
[8] Zhao J, Jiang P, Geng S, Guo L, Wang Y, Xu B. Experimental and numerical study on the effect of increasing frequency on the morphology and microstructure of aluminum alloy in laser wobbling welding. J Mater Res Technol 2022;21:267–82. https://doi.org/10.1016/j.jmrt.2022.09.008.
[9] Kraetzsch M, Standfuss J, Klotzbach A, Kaspar J, Brenner B, Beyer E. Laser beam welding with high-frequency beam oscillation: welding of dissimilar materials with brilliant fiber lasers. In: International congress on applications of lasers & electro-optics. 1. Laser Institute of America; 2011. p. 169–78. https://doi.org/10.2351/1.5062231.
[10] Khodabakhshi F, Shah LH, Gerlich AP. Dissimilar laser welding of an AA6022-AZ31 lap-joint by using Ni-interlayer: novel beam-wobbling technique, processing parameters, and metallurgical characterization. Optics Laser Technol 2019;112:349–62. https://doi.org/10.1016/j.optlastec.2018.11.034.
[11] Kumar D, Sarkar NS, Acherjee B, Kuar AS. Beam wobbling effects on laser transmission welding of dissimilar polymers: experiments, modeling, and process optimization. Optics Laser Technol 2022;146:107603. https://doi.org/10.1016/j.optlastec.2021.107603.
[12] Hernando Arriandiaga I, Arrizubieta Arrate JI, Lamikiz Mentxaka A, Arrien EU. Laser welding depth evaluation by means of an analytic model. DYNA-Ing Ind 2020;95(4):1–8.
[13] Chen X, Jiang N, Jiang M, Du Y, Ma S, Chen Y, et al. Numerical investigation of asymmetric weld fusion geometry in laser welding of aluminium alloy with beam oscillation. Science and Technology of Welding and Joining 2022;27(8):595–605. https://doi.org/10.1080/13621718.2022.2091343.
[14] Rai R, Elmer JW, Palmer TA, DebRoy T. Heat transfer and fluid flow during keyhole mode laser welding of tantalum, Ti–6Al–4V, 304L stainless steel and vanadium. J Phys D Appl Phys 2007;40(18):5753. https://doi.org/10.1088/0022-3727/40/18/037.
[15] Blecher JJ, Palmer TA, Debroy T. Porosity in thick section alloy 690 welds–experiments, modeling, mechanism, and remedy. Weld J 2016;95(1):17s–26s.
[16] Rai R, Roy GG, DebRoy T. A computationally efficient model of convective heat transfer and solidification characteristics during keyhole mode laser welding. J Appl Phys 2007;101(5):054909. https://doi.org/10.1063/1.2537587.
[17] Rai R, Kelly SM, Martukanitz RP, DebRoy T. A convective heat-transfer model for partial and full penetration keyhole mode laser welding of a structural steel. Metall Mater Trans A 2008;39:98–112. https://doi.org/10.1007/s11661-007-9400-6.
[18] Wei HL, Elmer JW, DebRoy T. Crystal growth during keyhole mode laser welding. Acta Mater 2017;133:10–20. https://doi.org/10.1016/j.actamat.2017.04.074.

[19] De A, DebRoy T. A smart model to estimate effective thermal conductivity and viscosity in the weld pool. J Appl Phys 2004;95(9):5230–40. https://doi.org/10.1063/1.1695593.
[20] De A, DebRoy T. Probing unknown welding parameters from convective heat transfer calculation and multivariable optimization. J Phys D Appl Phys 2003;37(1):140.
[21] Jiang M, Chen YB, Chen X, Tao W, Debroy T. Enhanced penetration depth during reduced pressure keyhole-mode laser welding. Weld J 2020;99:110–24. https://doi.org/10.29391/2020.99.011.
[22] Mondal B, Mukherjee T, Finch NW, Saha A, Gao MZ, Palmer TA, et al. Vapor pressure versus temperature relations of common elements. Materials 2022;16(1):50. https://doi.org/10.3390/ma16010050.
[23] Mondal B, Gao M, Palmer TA, DebRoy T. Solidification cracking of a nickel alloy during high-power keyhole mode laser welding. J Mater Process Technol 2022;305:117576. https://doi.org/10.1016/j.jmatprotec.2022.117576.
[24] Wang Z, Oliveira JP, Zeng Z, Bu X, Peng B, Shao X. Laser beam oscillating welding of 5A06 aluminum alloys: microstructure, porosity and mechanical properties. Optics Laser Technol 2019;111:58–65. https://doi.org/10.1016/j.optlastec.2018.09.036.
[25] Yang H, Jing G, Gao P, Wang Z, Li X. Effects of circular beam oscillation technique on formability and solidification behaviour of selective laser melted Inconel 718: from single tracks to cuboid samples. J Mater Sci Technol 2020;51:137–50. https://doi.org/10.1016/j.jmst.2019.09.044.
[26] Wang L, Gao M, Zhang C, Zeng X. Effect of beam oscillating pattern on weld characterization of laser welding of AA6061-T6 aluminum alloy. Mater Des 2016;108:707–17. https://doi.org/10.1016/j.matdes.2016.07.053.
[27] Zheng B, Zhou Y, Smugeresky JE, Schoenung JM, Lavernia EJ. Thermal behavior and microstructure evolution during laser deposition with laser-engineered net shaping: part II. Experimental investigation and discussion. Metall Mater Trans A 2008;39:2237–45. https://doi.org/10.1007/s11661-008-9566-6.
[28] Blecher JJ, Palmer TA, DebRoy T. Solidification map of a nickel-base alloy. Metall Mater Trans A 2014;45:2142–51. https://doi.org/10.1007/s11661-013-2149-1.
[29] Nawrocki J, Motyka M, Szeliga D, Ziaja W, Cygan R, Sieniawski J. Effect of cooling rate on macro-and microstructure of thin-walled nickel superalloy precision castings. J Manuf Process 2020;49:153–61. https://doi.org/10.1016/j.jmapro.2019.11.028.
[30] Mullis AM, Farrell L, Cochrane RF, Adkins NJ. Estimation of cooling rates during close-coupled gas atomization using secondary dendrite arm spacing measurement. Metall Mater Trans B 2013;44:992–9. https://doi.org/10.1007/s11663-013-9856-2.

Tuhin Mukherjee is a Postdoctoral Researcher at the Pennsylvania State University and author of many papers in leading journals including Nature Reviews Materials, Nature Materials, and Progress in Materials Science. He edited a book entitled "The Science and Technology of 3D Printing" (MDPI, 2021) and a textbook on "Theory and Practice of Additive Manufacturing" (Wiley, 2023). He served as a Guest Editor for the journals "Computational Materials Science", "Materials", and "Science and Technology of Welding and Joining". He is an Editorial Board Member of the journal "Science and Technology of Welding and Joining" and "Welding Journal".

Mingze Gao is a doctoral student at the Department of Engineering Science and Mechanics at the Pennsylvania State University. His primary research interests are laser welding, defect formation mechanisms, characterization techniques, powder production, and establishing the process-structure-property relationships during the processing of metallic materials using experimental and numerical tools.

Todd A. Palmer holds a joint appointment as a Professor of Engineering Science and Mechanics and Materials Science and Engineering and is the director of the Center for Innovative Sintered Products at The Pennsylvania State University. Before joining Penn State, he was at Lawrence Livermore National Laboratory as a metallurgist in the Materials Science and Technology Division. He is a Fellow of the American Welding Society and served as a Chair of the American Welding Society C7 Committee and D20 Committee and Penn State chapter of ASM International. He is also an editorial board member of "Journal of Materials Engineering and Performance" and "Science and Technology of Welding and Joining".

Tarasankar DebRoy is a Professor of Materials Science and Engineering at Penn State and the author of two books including a 2023 Wiley textbook on "Theory and Practice of Additive Manufacturing", five edited books, and over 380 well-cited technical articles. His work has been recognized by over 20 scholastic awards including a Fulbright Distinguished Chair from the US State Department, UK Royal Academy of Engineering's Distinguished Visiting Fellowship, and Penn State's Faculty Scholar medal. He served as a Distinguished Visiting Professor at IIT Bombay, Aditya Birla Chair at IISc, Bangalore, and Visiting Professor at AUST, Nigeria, KTH, Stockholm, and University West, Trollhattan, Sweden. He is a Founding Editor of the journal "Science and Technology of Welding and Joining".